Supporting information

Magnetized MXene microspheres with multi-scale magnetic coupling and enhanced polarized interfaces for distinct microwave absorption via a spray-drying method

*Xiao Li[a, 1], Mao Zhang[a, 1], Wenbin You[a], Ke Pei[a], Qingwen Zeng[a], Qing Han[a], Yuesheng Li[a], Hui Cao[a], Xianhu Liu[b], Renchao Che[a, *].*

[a]Laboratory of Advanced Materials, Department of Materials Science and Collaborative Innovation Center of Chemistry for Energy Materials (iChem), Fudan University, Shanghai 200438, P. R. China

*E-mail: rcche@fudan.edu.cn

[b]Key Laboratory of Materials Processing and Mold (Zhengzhou University), Ministry of Education, Zhengzhou 450002, P. R. China

[1]These authors contributed equally to this work.

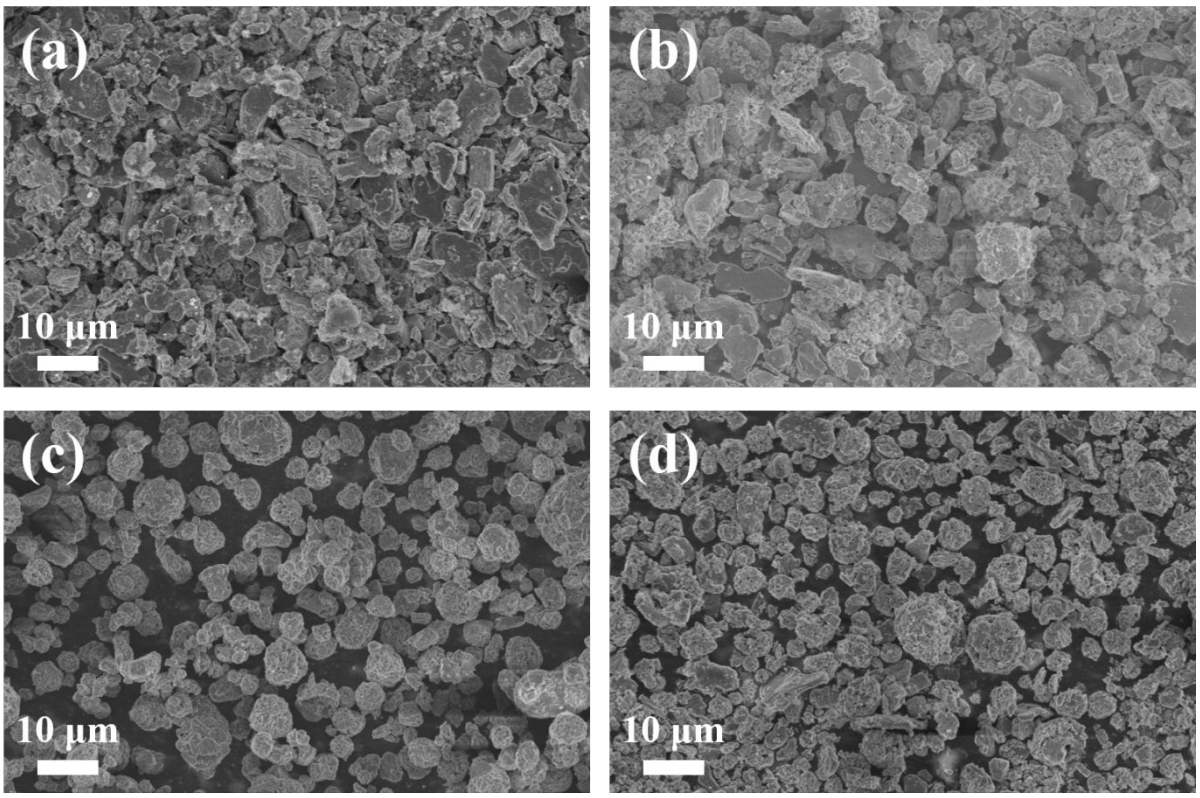

Figure S1. SEM images of preparation M/F composites at lower temperature (a, b), at higher suspension concentration (c, d).

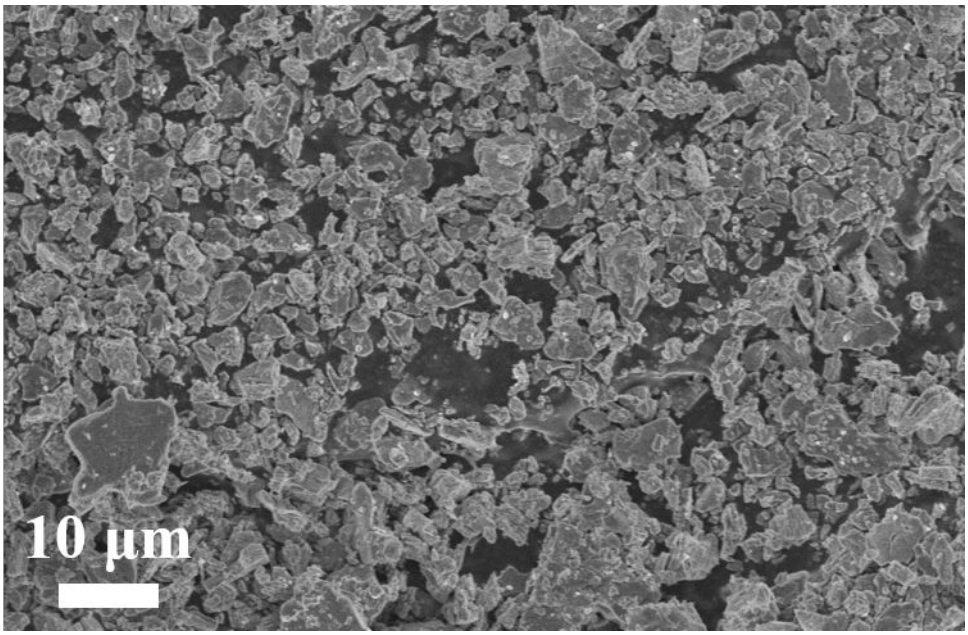

Figure S2. SEM image of accordion-like MXene after the ultrasonic cell disrupting.

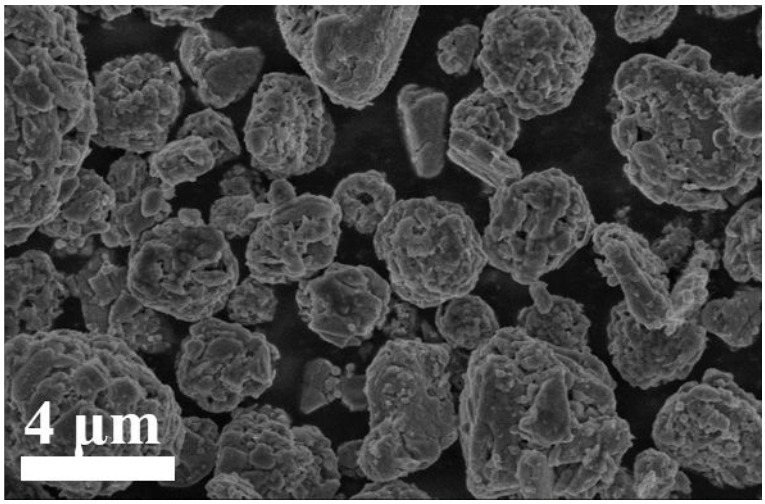

Figure S3. SEM image of M/F composites.

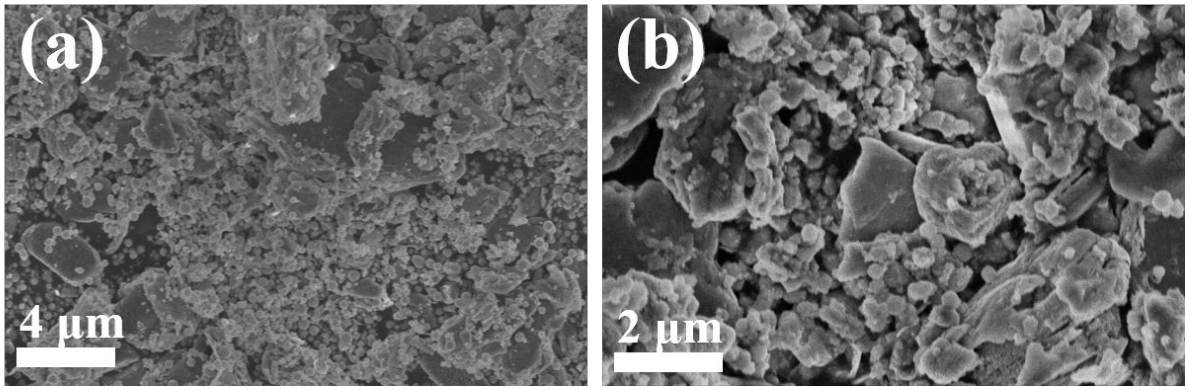

Figure S4. SEM images of M/F-m sample at lower magnification (a) and higher magnification (b).

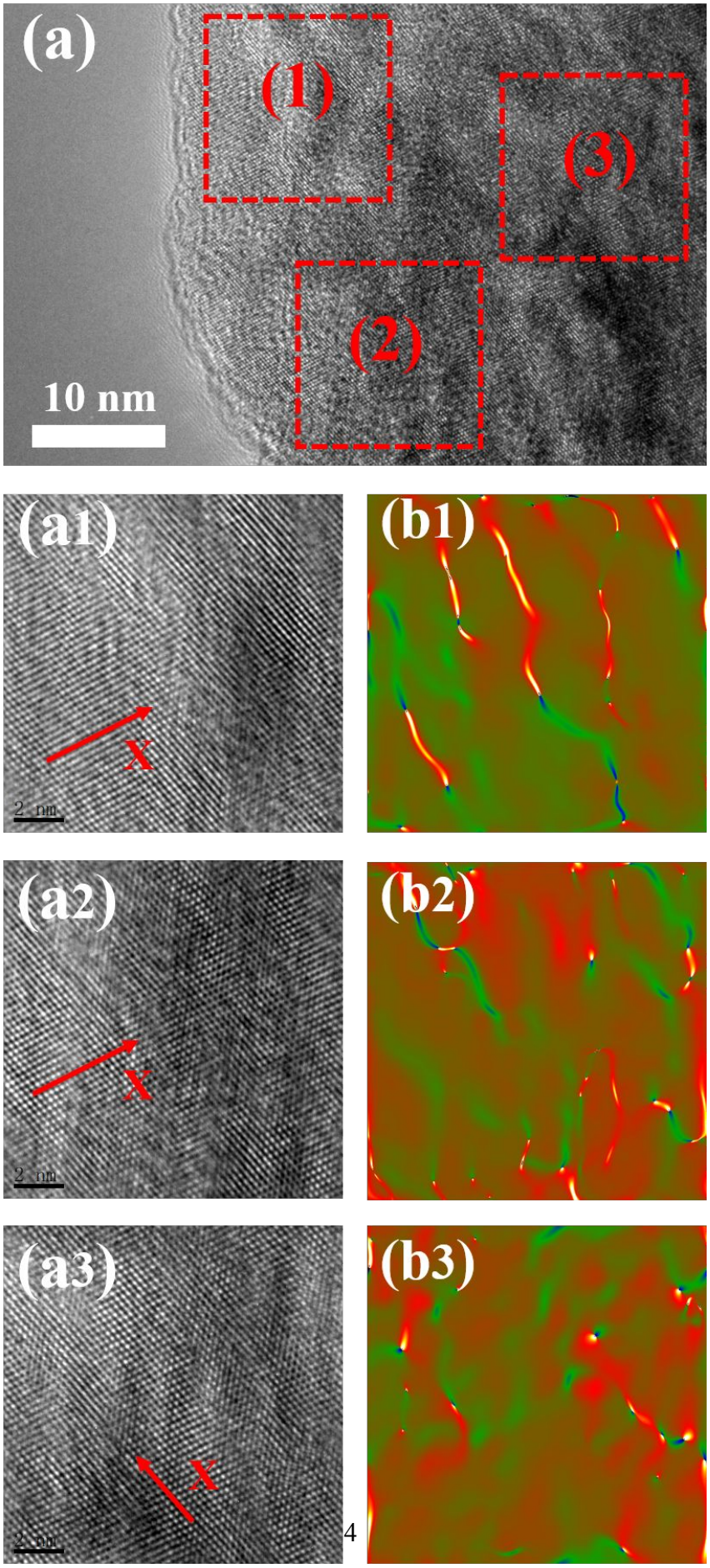
(a)
(1)
(2)
(3)
10 nm
(a1)
X
2 nm
(b1)
(a2)
X
2 nm
(b2)
(a3)
X
2 nm
(b3)

Figure S5. HRTEM image of MXene nanosheets (a); corresponding areas (a1, a2 and a3) and corresponding strain maps (b1, b2 and b3) of the MXene nanosheets. The color variation indicated the strain values ranging from -0.7 to 0.7.

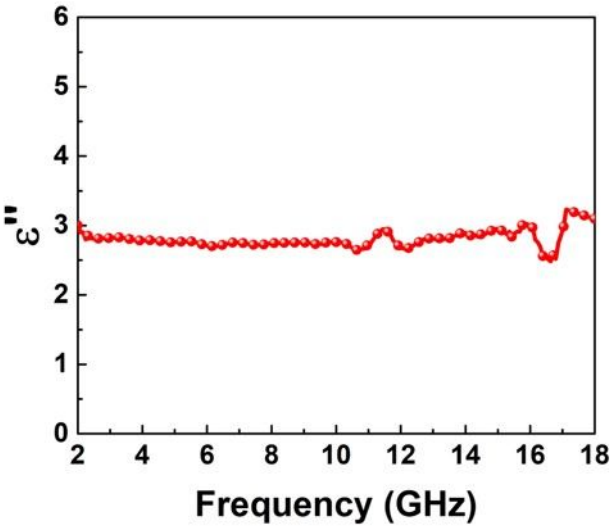

Figure S6. ε″ value versus frequency of M/F composite.

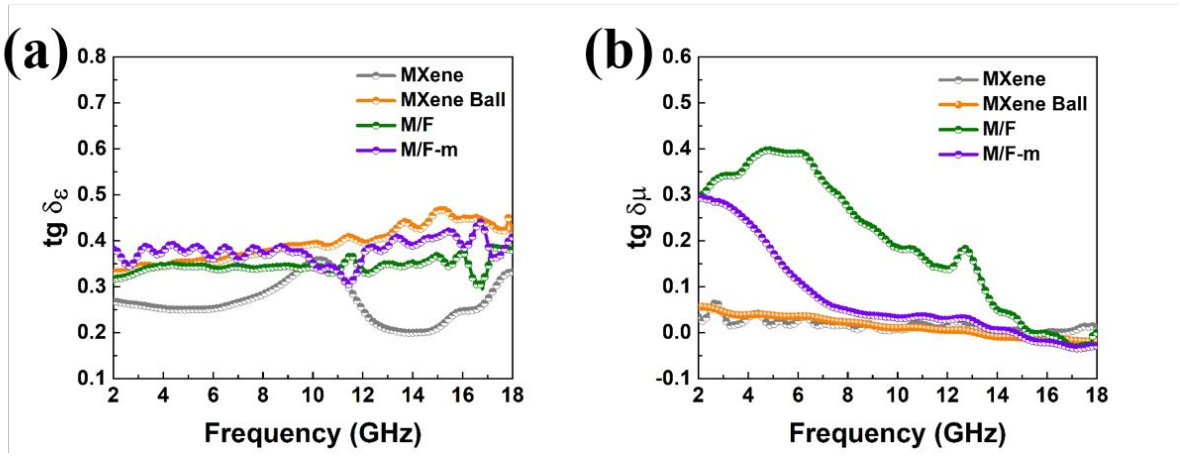

Figure S7. Dielectric loss tangent (a) and magnetic loss tangent (b) versus frequency of four different samples.

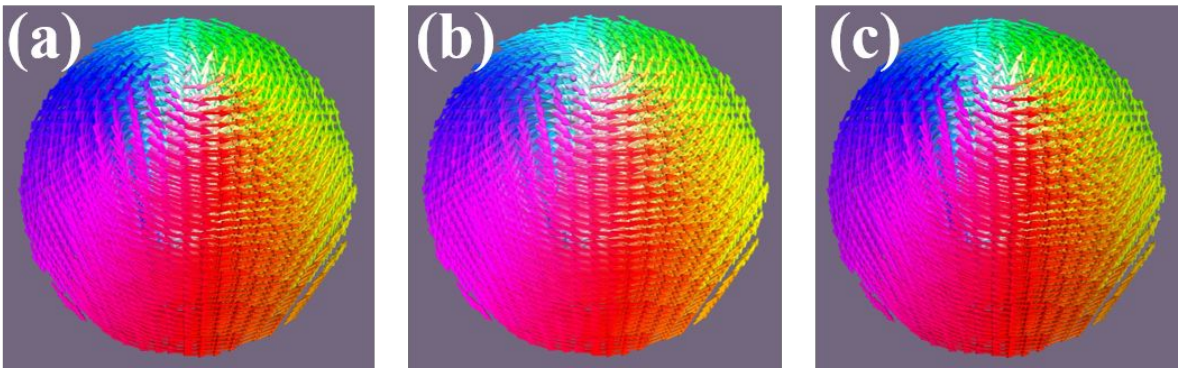

Figure S8. The cyclical variation of magnetic moments of the individual Fe_3O_4 nanosphere under an alternating magnetic field obtained from computational micromagnetic simulation (a, b and c). The size of single Fe_3O_4 nanosphere is 250nm. The frequency of external magnetic field is 2 GHz.

Table S1. Comparison of microwave absorption performance among the reported MXene-based composites, Fe_3O_4-based composites and the as-prepared M/F composites.

Absorber	RL_{min} (dB)	Matching frequency (GHz)	EAB (GHz)	Thickness (mm)	refs
MXene/amorphous carbon/TiO_2	-48.4	11.6	2.8	1.85	S1
MXene/ZnO	-26.3	17.4	1.4	4	S2
MXene/$Ni_{0.5}Zn_{0.5}Fe_2O_4$	-42.5	13.5	3	6.5	S3
MXene/PVB/$Ba_3Co_2Fe_{24}O_{41}$	-46.3	5.8	1.6	2.8	S4
MXene/Ni-modified	-18.2	16.2	6.3	1.5	S5
MXene/Co_3O_4	-34.5	14	6.3	2.0	S6

MXene/FeCo	-17.86	-	8.8	1.6	S7
MXene/CoFe	-36.29	8.56	2.64	2.2	S8
MXene/TiO_2/MoS_2	~ -16	~ 9.8	2.6	2.5	S9
MXene/Fe_3O_4/PANI	-40.3	15.3	5.2	1.9	S10
MXene/Ni chain	-49.9	11.9	2.1	1.75	S11
MXene/carbonyl iron	-15.52	12.8	8.16	1	S12
Fe_3O_4	-53.0	2.2	<2	4	S13
Fe_3O_4/C	-40	16	-	1.5	S14
MXene/Fe_3O_4	**-50.6**	**13.5**	**4.67**	**2**	**this work**

References

S1. Han, M.; Yin, X.; Wu, H.; Hou, Z.; Song, C.; Li, X.; Zhang, L.; Cheng, L., Ti_3C_2 MXenes with Modified Surface for High-Performance Electromagnetic Absorption and Shielding in the X-Band. *ACS Appl. Mater. Interfaces* 2016, 8, 21011-21019.

S2. Qian, Y.; Wei, H.; Dong, J.; Du, Y.; Fang, X.; Zheng, W.; Sun, Y.; Jiang, Z., Fabrication of Urchin-like ZnO-MXene Nanocomposites for High-performance Electromagnetic Absorption. *Ceramics International* 2017, 43, 10757-10762.

S3. Li, Y.; Zhou, X.; Wang, J.; Deng, Q.; Li, M.; Du, S.; Han, Y. H.; Lee, J.; Huang, Q., Facile Preparation of In-situ Coated $Ti_3C_2T_x$/$Ni_{0.5}Zn_{0.5}Fe_2O_4$ Composites and Their Electromagnetic Performance. *RSC Adv.* 2017, 7, 24698-24708.

S4. Yang, H.; Dai, J.; Liu, X.; Lin, Y.; Wang, J.; Wang, L.; Wang, F., Layered PVB/$Ba_3Co_2Fe_{24}O_{41}$/Ti_3C_2 MXene Composite: Enhanced Electromagnetic

Wave Absorption Properties with High Impedance Match in a Wide Frequency Range. *Materials Chemistry and Physics* 2017, 200, 179-186.

S5. Feng, W.; Luo, H.; Zeng, S.; Chen, C.; Deng, L.; Tan, Y.; Zhou, X.; Peng, S.; Zhang, H., Ni-modified Ti_3C_2 MXene with Enhanced Microwave Absorbing Ability. *Materials Chemistry Frontiers* 2018, 2, 2320-2326.

S6. Deng, R.; Chen, B.; Li, H.; Zhang, K.; Zhang, T.; Yu, Y.; Song, L., MXene/Co_3O_4 Composite Material: Stable Synthesis and its Enhanced Broadband Microwave Absorption. *Applied Surface Science* 2019, 488, 921-930.

S7. He, J.; Shan, D.; Yan, S.; Luo, H.; Cao, C.; Peng, Y., Magnetic FeCo Nanoparticles-decorated Ti_3C_2 MXene with Enhanced Microwave Absorption Performance. *J. Magn. Magn. Mater*. 2019, 4921-4926.

S8. Zhou, C.; Wang, X.; Luo, H.; Deng, L.; Wang, S.; Wei, S.; Zheng, Y.; Jia, Q.; Liu, J., Interfacial Design of Sandwich-like CoFe@$Ti_3C_2T_x$ Composites as High Efficient Microwave Absorption Materials. *Applied Surface Science* 2019, 494, 540-550.

S9. Wang, H.; Ma, H., The Electromagnetic and Microwave Absorbing Properties of MoS_2 Modified $Ti_3C_2T_x$ Nanocomposites. *J. Mater. Sci. Mater. Electron*. 2019, 30, 15250-15256.

S10. Wang, Y.; Gao, X.; Zhang, L.; Wu, X.; Wang, Q.; Luo, C.; Wu, G., Synthesis of Ti_3C_2/Fe_3O_4/PANI Hierarchical Architecture Composite as an Efficient Wide-band Electromagnetic Absorber. *Applied Surface Science* 2019, 480, 830-838.

S11. Liang, L.; Han, G.; Li, Y.; Zhao, B.; Zhou, B.; Feng, Y.; Ma, J.; Wang, Y.; Zhang, R.; Liu, C., Promising $Ti_3C_2T_x$ MXene/Ni Chain Hybrid with Excellent Electromagnetic Wave Absorption and Shielding Capacity. *ACS Appl. Mater. Interfaces* 2019, 11, 25399-25409.

S12. Yan, S.; Cao, C.; He, J.; He, L.; Qu, Z., Investigation on the Electromagnetic and Broadband Microwave Absorption Properties of Ti_3C_2 MXene/Flaky Carbonyl Iron Composites. *J. Mater. Sci. Mater. Electron*. 2019, 30, 6537-6543.

S13. Sun, G. B.; Dong, B. X.; Cao, M. H.; Wei, B. Q.; Hu, C. W., Hierarchical Dendrite-Like Magnetic Materials of Fe_3O_4, gamma-Fe_2O_3, and Fe with High Performance of Microwave Absorption. *Chem. Mat.* 2011, 23, 1587-1593.

S14. Du, Y.; Liu, W.; Qiang, R.; Wang, Y.; Han, X.; Ma, J.; Xu, P., Shell Thickness-Dependent Microwave Absorption of Core-Shell Fe_3O_4@C Composites. *ACS Appl. Mater. Interfaces* 2014, 6, 12997-13006.

The basic principle of geometric phase analysis is as follows:

For a perfect crystal, a HRTEM can be described as a Fourier series:

$$\mathrm{I(r)} = \sum_g H_g e^{2\pi i g \cdot r} \quad (1)$$

Where I(r) is the image intensity at the position r, g is the periodicities of the Bragg reflections, the Fourier coefficients H_g can be described as:

$$\mathrm{H(g)} = A_g e^{ip_g} \quad (2)$$

Where A_g is the amplitude of the set of sinusoidal lattice fringes g, P_g is the lateral position of the fringes in the original image.

In real image conditions, the Fourier coefficient H_g has conjugate symmetry. Image strength can be expressed as the following real number function:

$$\mathrm{I(r)} = A_0 + \sum_{g>0} 2A_g \cos\left(2\pi g \cdot r + p_g\right) \quad (3)$$

When processing the actually captured high-resolution image, the lattice image is subjected to fast Fourier transform processing to obtain an inverted space bitmap. A

specific $\pm$ g direction lattice is selected by a mask to obtain a specific direction stripe information, and then an inverse Fourier transform is performed to obtain a lattice fringe $B_g(r)$ in the specific direction:

$$B_g(r) = 2A_g \cos\left(2\pi g \cdot r + p_g\right) \quad (4)$$

In order to describe the lattice changes caused by distortion and defects in the material, the amplitude and phase of the lattice fringes should be expressed by the functions $A_g(r)$ and $P_g(r)$ for the position π, which should be written as:

$$B_g(r) = 2A_g(\mathrm{r}) \cos\left(2\pi g \cdot r + p_g(r)\right) \quad (5)$$